remote sensing

MDPI

Technical Note

The Analysis of Cones within the Tianwen-1 Landing Area

Hai Huang [1,2], Jianjun Liu [1,2,*], Xing Wang [1,2], Yuan Chen [1,2], Qing Zhang [1,2], Dawei Liu [1], Wei Yan [1] and Xin Ren [1]

[1] Key Laboratory of Lunar and Deep Space Exploration, National Astronomical Observatories, Chinese Academy of Sciences, Beijing 100101, China; huangh@nao.cas.cn (H.H.); wangx01@nao.cas.cn (X.W.); cheny@nao.cas.cn (Y.C.); zhangq@nao.cas.cn (Q.Z.); liudw@nao.cas.cn (D.L.); yanw@nao.cas.cn (W.Y.); renx@nao.cas.cn (X.R.)

[2] School of Astronomy and Space Science, University of Chinese Academy of Sciences, Beijing 100049, China

* Correspondence: liujj@nao.cas.cn

Abstract: On 15 May 2021, the Zhurong rover of China's first Mars mission, Tianwen-1 (TW-1), successfully landed in southern Utopia Planitia on Mars. Various landforms were present in the landing area, and this area recorded a complex geological history. Cones are one of the typical landforms in the landing area and Utopia Planitia, and they have a great significance to the local geological processes due to the diversity of their origins. Using High-Resolution Imaging Camera (HiRIC) images collected by the TW-1 orbiter, we identified a total of 272 well-preserved circular cones in the landing area. Detailed surveys of their spatial distribution, morphological characteristics, and morphometric parameters were conducted. A preliminary analysis of the surface characteristics of these cones also provides additional information to strengthen our understanding of them. The results of the high-resolution topographic analysis show that the cone heights are in the range of 10.5–90.8 m and their basal diameters range from 178.9–1206.6 m. We compared the morphometric parameters of the cones in the landing area with terrestrial and Martian analogous features and found that our measured cones are consistent with the ranges of mud volcanoes and also a small subset of igneous origin cones. However, the result of spatial analysis is more favorable to mud volcanoes, and the lower thermal inertia of the cones in the landing area compared to their surrounding materials is also a typical characteristic of mud volcanoes. Based on current evidence and analysis, we favor interpreting the cones in the TW-1 landing area as mud volcanoes.

Keywords: Tianwen-1; cones; Utopia Planitia; Mars; mud volcano

Citation: Huang, H.; Liu, J.; Wang, X.; Chen, Y.; Zhang, Q.; Liu, D.; Yan, W.; Ren, X. The Analysis of Cones within the Tianwen-1 Landing Area. *Remote Sens.* **2022**, *14*, 2590. https://doi.org/10.3390/rs14112590

Academic Editor: Roberto Orosei

Received: 22 March 2022
Accepted: 25 May 2022
Published: 27 May 2022

1. Introduction

Cone-like features are common landforms on Mars, and they have been reported in Viking images since the early days of Mars exploration [1,2]. There is a variety of mechanisms to produce these Martian cones, including interpretations as mud volcanoes [3–6], tuff rings/cones [7], pingos [8,9], cinder/scoria cones [10,11], and rootless cones [12,13]. Thus, it is impossible to conclude the origin of cones in a single geological process [14]. Cones on Mars have a wide range of morphometric parameters, and different origins of cones could be very similar in geometry. They can be found in many regions on Mars, including high-latitude areas [15], making the analysis more complex. Different geological processes can create similar landforms [16], leading to multiple plausible interpretations of the same feature and the complexity of interpreting these features by remote sensing detections [8]. In addition, there are different interpretations of the cones even in the same region on Mars. For example, cones in Isidis Planitia are interpreted as cinder/scoria cones [17], rootless cones [18], and mud volcanoes [19]. The origins of cones in some regions on Mars are still under discussion, especially in areas with complex geological evolution, but in general, three significant origins have been suggested for the cones on Mars, including volcanic/igneous, ground-ice, and sedimentary processes [11].

Utopia Planitia on Mars is known as an ancient circular impact basin occupying a vast area of Martian northern lowlands [20,21]. Previous studies have identified various landforms in Utopia Planitia, including giant polygons and polygonal terrain [22–25], mud volcanoes [26], igneous cones [27], pancake/rampart craters [6], and periglacial features [28]. These recorded features reflect a complex geological history in Utopia Planitia. In fact, there were volcanic, glacial, fluvial, and sedimentary processes in Utopia Planitia [6,26–30]. Head et al. [30] proposed that the northern lowlands were ridged plains of volcanic origin based on topographic analyses. The Martian ancient northern ocean hypothesis [31–33] is a key geological setting of Utopia Planitia and is still an open issue. Moreover, the widespread Vastitas Borealis Formation (VBF), generally viewed as the product of the water-related sedimentary activity [33–35], covered the bulk of the northern lowlands. Thus, the complex geological history of Utopia Planitia makes the research on the origin of the landforms (including cones) in this region uncertain.

The TW-1 landing area, located on the southern edge of Utopia Planitia, is near the highland-lowland boundary (Figure 1). The Zhurong rover landed at 109.925° E and 25.066° N [36]. This paper takes the TW-1 landing area as our study area, and we surveyed the cones in the landing area. Many landforms appear in the landing area, and this region has a complex geological history [36]. Cones in Utopia Planitia also have different origins [8,26,27]. Therefore, the study of the landing area cones is essential not only for accessing the local geological evolution history but also for insight into the early climate on Mars. In addition, the analysis of cones on mars has a significant implication for astrobiology, such as the possible indicators of methane or microorganisms [37,38].

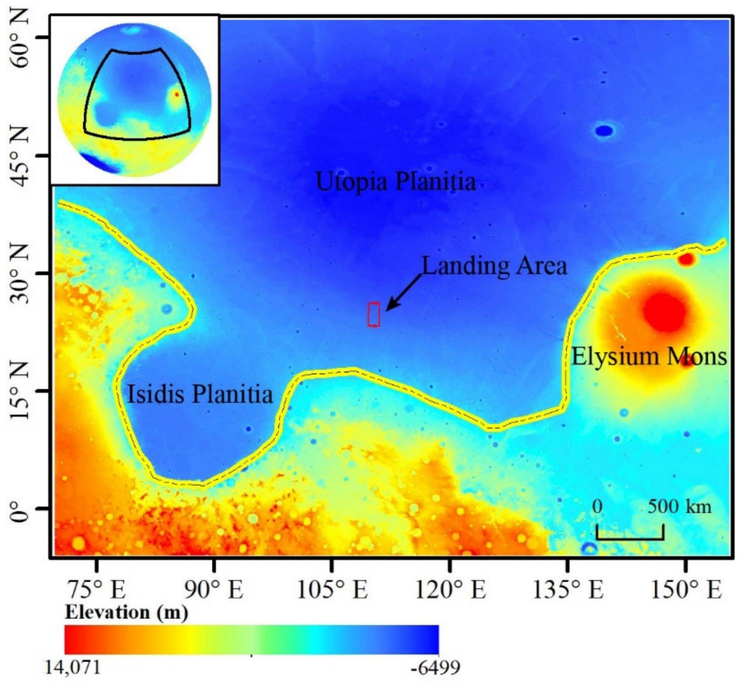

Figure 1. The location of the Tianwen −1 landing area (denoted by red line). The bold yellow line indicates the highland-lowland boundary. The base map is MOLA DEM.

This paper aims to conduct a quantitative analysis of the cones in the landing area based on the HiRIC datasets and other orbital image data. We performed various analyses (e.g., morphometric analysis, spatial analysis, etc.) for the cones in the landing area and compared these cones with terrestrial and Martian analogous features. In Section 2, the dataset and the method used in this study are introduced. The results and discussion are presented in Section 3. Our conclusions are presented in Section 4.

2. Data and Methods

HiRIC onboard on TW-1 orbiter has been imaging the Martian surface before the Zhurong rover touched down in southern Utopia Planitia. HiRIC can obtain both panchromatic and color images [39]. In this paper, all of the used images are panchromatic images (0.45–0.9 μm). We have acquired enough HiRIC forward and backward stereo image coverage over the landing area. These images were acquired at an orbital height of 350 km with a spatial resolution of ~0.7 m [36]. The high-resolution HiRIC-derived digital orthophoto map (DOM, spatial resolution of ~0.7 m/pixel) and digital elevation model (DEM, spatial resolution of ~3.5 m/pixel) were obtained from these stereo images [36]. We used the HiRIC-derived DOM and DEM to survey the morphology of the cones in the landing area. The high-resolution inertia data (spatial resolution of ~100 m/pixel) derived from the Thermal Emission Imaging System (THEMIS) were also used to survey the thermophysical properties of the landing area surface. All these remote sensing datasets were integrated into a Geographic Information System (GIS) using the ArcMap software.

The nearest-neighbor (NN) analysis is an effective method for studying Martian small features (e.g., small cones, domes, mounds, impact craters, etc.) [5,40–43]. The NN technique was used in this work to conduct a comparative study on cones within the landing area and their analogous features. When performing NN analysis, every feature is represented by a spatial point in a map or image. In accordance with references [41,44], the NN methodology is summarized as follows:

The nearest neighbor ratio is given as:

$$R = \frac{R_a}{R_e}, \tag{1}$$

where R_a is the observed mean distance between each feature and its nearest neighbor:

$$R_a = \frac{\sum_{i=1}^{n} r_i}{n}, \tag{2}$$

and R_e is the expected mean distance for the features given in a random pattern:

$$R_e = \frac{0.5}{\sqrt{\rho}}, \tag{3}$$

In the above equations, r_i equals the distance between feature i and its nearest neighbor, n equals the total number of features in the feature field, and ρ is the density of the feature field (i.e., number of features divided by field area). In this study, the field area is the area of a minimum enclosing rectangle around all features. By definition, large values of NN ratios ($R > 1$) indicate that features could be random in their spatial distribution and conversely clustered.

The *c-score* is the key test statistic for evaluating whether an observed distribution is consistent with a random Poisson distribution:

$$c = \frac{R_a - R_e}{\sigma R_e}, \tag{4}$$

where σR_e is the standard error of the mean of the NN distances in a randomly distributed population. By definition, if $|c| > 1.96$, it can indicate a statistically significant nonrandomness at the 0.05 significance level.

Burno et al. [41] examined the skewness-kurtosis relation of pairwise NN distances to distinguish small geological features better. Skewness is a measure of asymmetry. A positive skewness value indicates data skewed to the right, and a negative skewness value indicates data skewed to the left. Kurtosis describes the shape of a distribution. A higher kurtosis value indicates a distribution with a sharper and higher peak. We also calculated the skewness and kurtosis in this study. Following are standard formulations:

$$Skewness = \frac{n}{(n-1)(n-2)} \sum_{i=1}^{n} \left(\frac{r_i - R_a}{s} \right)^3, \quad (5)$$

$$Kurtosis = \frac{n(n+1)}{(n-1)(n-2)(n-3)} \sum_{i=1}^{n} \left(\frac{r_i - R_a}{s} \right)^4 - \frac{3(n-1)^2}{(n-2)(n-3)}, \quad (6)$$

where s is the sample standard deviation of the pairwise NN distance in the feature field.

3. Results and Discussion

3.1. Morphometric Analysis

Quantifying the geometry of the cones is the first step to understanding these features. We identified 272 circular cones in the landing area using HiRIC-derived DEM and DOM and measured the morphometric parameters of these cones (see Table S1 in Supplementary Materials). Figure 2a shows the three-dimensional (3D) reconstruction result of the cones in the landing area. They are truncated cones with central summit depressions. We used the following morphometric parameters (Figure 2b) to characterize the landing area cones: cone width (i.e., basal diameter) (Wco), crater width (Wcr), and cone height (Hco). To acquire accurate morphometric parameters, the topographic profiles passing through the center of a cone in four different directions were measured using HiRIC-derived DEM (Figure 2c,d), and then their average topographic profiles were used to obtain the morphometric parameters. These basal parameters and their derived parameters (e.g., Hco/Wco, Wcr/Wco) are commonly used to study small features on both Earth and Mars [3,7,10,45–47].

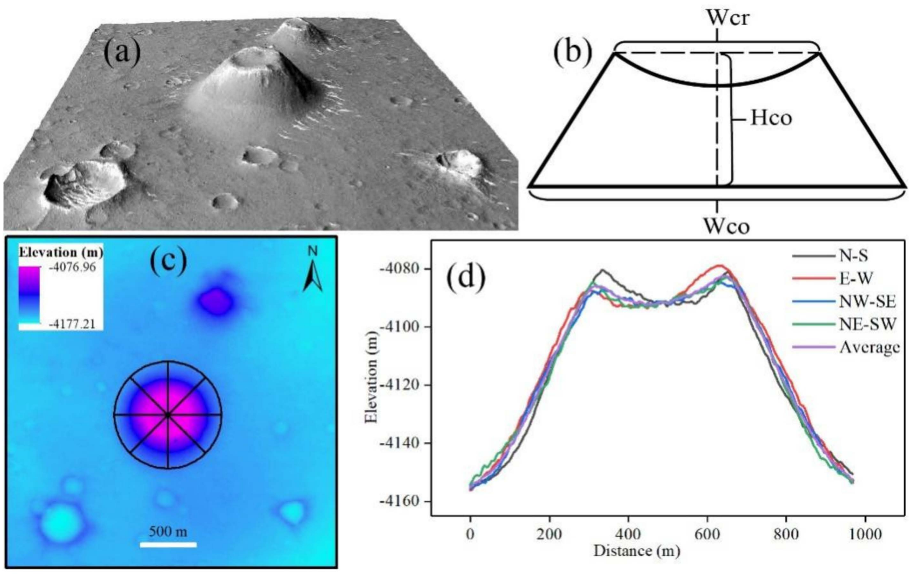

Figure 2. (**a**) Example of 3D reconstruction result of the landing area cones. (**b**) Schematic diagram of the morphometric parameters of a cone. How we acquired the cone topographic profiles from HiRIC−derived DEM is shown in (**c**), and (**d**) is an example of calculating average profile of a cone based on topographic profiles in four directions.

The results of morphometric measurement (Figure 3) show that the range of Wco is 178.9–1206.6 m, with a mean of 468.3 m, the range of Wcr is 58–687.9 m, with a mean of 233.5 m, and the range of Hco is 10.5–90.8 m with a mean of 34.2 m. Figure 4 shows the frequency histograms and cumulative percentages of these three parameters. The mean, median, and mode of these three parameters indicate a positively skewed distribution of the cones in the landing area. Approximately 80% of our mapped cones have Wco < 550 m, Wcr < 300 m, and Hco < 40 m.

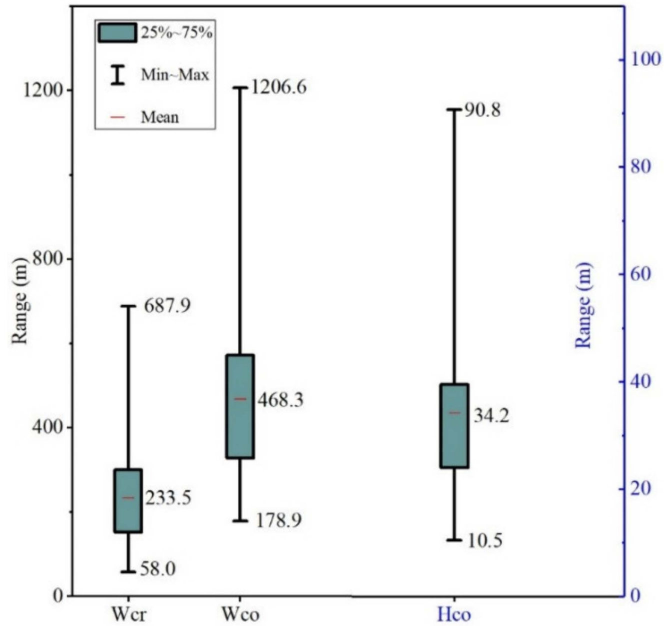

Figure 3. Box and whisker plots for three morphometric parameters data distributions of the landing area cones. Wcr and Wco refer to the left vertical axis, while Hco refers to the right vertical axis.

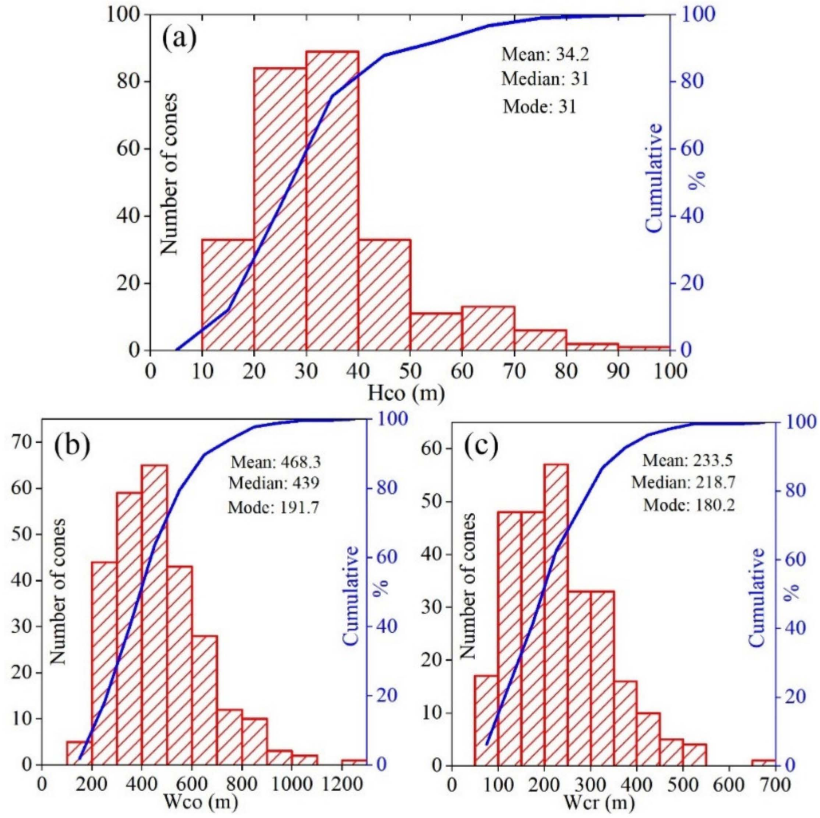

Figure 4. Frequency histograms and cumulative percentages of (**a**) cone height (Hco), (**b**) cone basal diameter (Wco), and (**c**) cone crater width (Wcr).

Morphological comparative analysis is a powerful tool to distinguish between multiple working hypotheses for Martian cone-like features. It should be noted that different environmental conditions on Mars and Earth may affect the formation processes of the cones [3]. For example, the different atmospheric and gravity conditions could make the flank of the cone shape differently on Mars [10]. Therefore, the morphometric comparison of the landing area cones with Martian analogs may be more convincing due to the similar environmental conditions, while the terrestrial analogs may also supply some references.

Their morphometric parameters of the landing area cones and the analogous features on Mars and Earth are summarized in Table 1. The three parameters of our measured cones can be found to be relatively consistent with those of some terrestrial and Martian analogous features (Figure 5). When compared with Martian analogous features (Figure 5a and Figure S1 in Supplementary Materials), we found that the landing area cones are similar in morphology to Martian mud volcanoes and pingos. Some of the compared analogous features (e.g., Martian tuff rings/cones, Martian rootless cones, Martian cinder/scoria cones) show morphometric parameters significantly different from the landing area cones. Thus, we favor that those compared analogous features are less possible origins of the landing area cones. However, we speculate that the landing area cones are less likely to be pingos because the cones in our study area have smooth surfaces and no cracks or fissures, which are supposed to be the typical characteristics of pingos [8], are observed at the top of the cones. The TW-1 landing area is located at low latitude (~23–26.5° N, see Figure 8a in Section 3.3), where the presence of shallow subsurface ice may not be stable [48,49]. Any pingos with ice cores [8], if they were, should be collapsed, and no positive relief would exist. Besides, the previously reported pingos in Utopia Planitia appear at relatively high latitudes (>35° N) rather than at the southern edge of Utopia Planitia [9,50,51]. Notably, the cones in our study area are strikingly similar to the Hephaestus Fossae cones on Mars in morphology, which were interpreted as pyroclastic cones [40]. When compared with terrestrial analogous features (Figure 5b and Figure S1 in Supplementary Materials), our measured cones in the landing area are most similar to pingos, subaqueous/subaerial mud volcanoes, cinder/scoria cones, and rootless cones (Figure 5b and Figure S1 in Supplementary Materials).

Table 1. A summary of morphometric parameters of the features shown in Figure 5.

Feature Type	N	Hco Range (Average) (m)	Wco Range (Average) (m)	Hco/Wco Range (Average)
		Mars		
Landing area cones	272	10.5–90.8 (34.2)	178.9–1206.6 (468.3)	0.0276–0.1696 (0.0765)
Cinder/scoria cones	28	75–573 (217.75)	928–7500 (2347)	0.0318–0.1432 (0.097)
Igneous cones	24	12–39 (23.92)	237–791 (458.67)	0.0307–0.0765 (0.05366)
Mud volcanoes	43	6–300 (33.52)	147–3000 (542.65)	0.0034–0.1429 (0.06571)
Pingos	8	300–1000 (550)	35–140 (63.125)	0.07–0.1667 (0.1231)
Rootless cones	-	0.3–10.52	6.7–105.6	-
Tuff rings/cones	38	35–372 (123.08)	3179–17,535 (7762.58)	0.0049–0.0371 (0.0168)
		Earth		
Cinder/scoria cones	39	30–300 (128.0769)	137–2000 (877.0256)	0.0248–0.5333 (0.1593)
Lava domes	16	15–200 (82.75)	45–800 (424.3125)	0.104–0.5137 (0.2129)
Maars	77	4–167 (34.36)	91–8750 (1899.69)	0.003–0.0984 (0.0237)
Subaqueous mud volcanoes	619	1.8–2364.86 (188.47)	142–42,000 (3025.94)	0.00625–0.3346 (0.0668)
Pingos	4	12–24 (19)	100–260 (165)	0.0923–0.16 (0.1231)
Rootless cones	10	4–29 (17)	42–355 (317.0909)	0.0629–0.2 (0.111)
Subaerial mud volcanoes	21	10–380 (154.2381)	150–6200 (2872.9524)	0.0257–0.1316 (0.06142)
Tuff rings/cones	43	10–345 (103.67)	541–3900 (1915.42)	0.0056–0.1504 (0.0595)

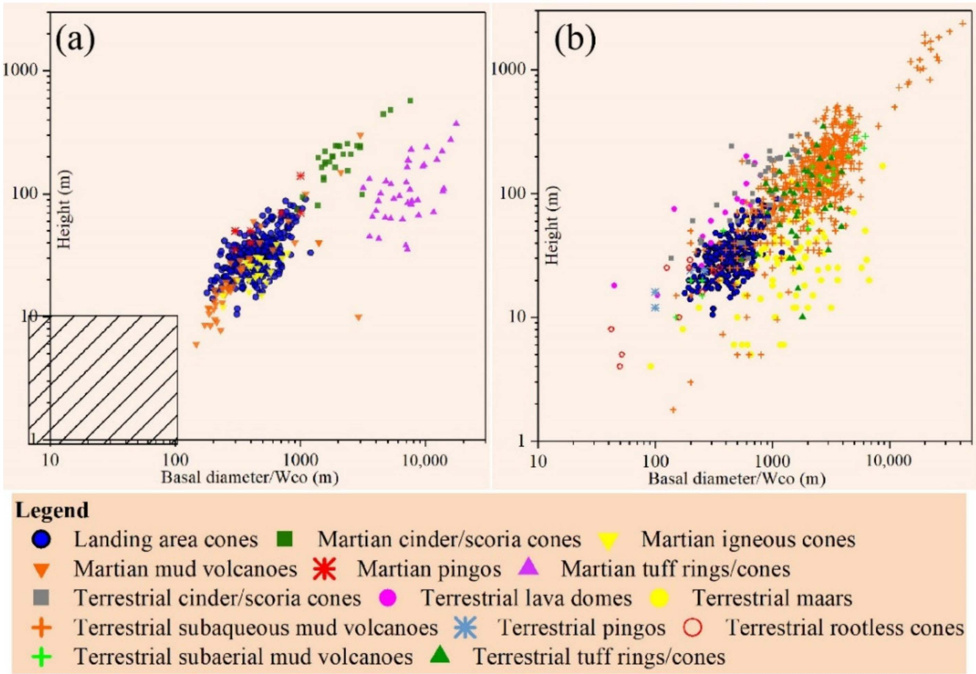

Figure 5. Log-log plots showing cone heights (Hco) versus basal diameters (Wco). All of the data are from previous studies, including Martian cinder/scoria cone [10], Martian igneous cone [40], Martian mud volcanoes [3,4], Martian pingos [52], Martian tuff rings/cones [7], terrestrial cinder/scoria cones [53–55], terrestrial lava domes [54], terrestrial maars [54], terrestrial subaqueous mud volcanoes [56,57], terrestrial pingos [52], terrestrial rootless cones [54], terrestrial subaerial mud volcanoes [7,58], and terrestrial tuff rings/cones [54]. (**a**) Morphometric comparison between the studied cones and the features on Mars. The bottom left rectangle with filled diagonals represents Martian rootless cones that were acquired from [12] (Wco: 2.7–105.6 m, Hco: 0.3–10.52 m). (**b**) Morphometric comparison between the studied cones and the features on Earth. A series of separate panels are provided in Figure S1 in Supplementary Materials to complement this figure for better understanding.

Here, we can initially exclude some candidate origins of the landing area cones based on the preliminary results of the morphometric analysis, including Martian rootless cones, Martian tuff rings/cones, and Martian cinder/scoria cones. Further analyses and discussions of the origins of the landing area cones are continued in the following sections.

3.2. Cone Characteristics

The cones in the landing area appear as isolation, clusters, and chains (see Figure S2 in Supplementary Materials), with isolated cones predominating. Both mud volcanoes and volcanic/igneous-related cones on Mars can occur in isolation, clusters, or as chains [59,60]. The landing area cones also have a similar appearance to volcanic/igneous-related cones (see Figure 3 of [40]) and mud volcanoes (see Figure 4 of [4]) on Mars. Most of the cones in the landing area have smooth, bright surfaces (Figure 6) and relatively low thermal inertia (TI) based on the THEMIS-derived thermal inertia map [61,62]. The TI (unit of J m^{-2} K^{-1} $s^{-1/2}$) provides significant insight into the physical nature of the surface and is uniquely related to an effective particle size [61]. Figure 7 shows the TI values of the surroundings of the Zhurong landing site, on which the cone fields (outlined by the green lines in Figure 7) present lower TI values (range of ~270.1–~354.5 J m^{-2} K^{-1} $s^{-1/2}$) than the surrounding plains, especially in the center of cones (avg. ~273.4 J m^{-2} K^{-1} $s^{-1/2}$). This implies that the construct-forming materials of these cones are mostly fine-grained materials [63]. Previous studies reported that Martian mud volcanoes have lower TI values than their local surroundings [4,64,65]. These relatively low TI values materials may be interpreted as mud (e.g., fine-grained sediments) rather than solidified lava (or consolidated carapace of ash/indurated tuff) with higher TI values [4]. The landing area cones have relatively low TI values and high albedo compared with the surroundings, and the possible explanation for this phenomenon is that the compositions of the landing area cones may include the dried, loosely cemented, fine-grained sediments/mud deposits, similar to other Martian mud volcanism fields [65,66]. However, it should be noted that some volcanic/igneous-related cones (e.g., tuff cones/rings) can also be formed by fine-grained materials, such as unconsolidated carapace of ash or volcanic ash deposits [61,65].

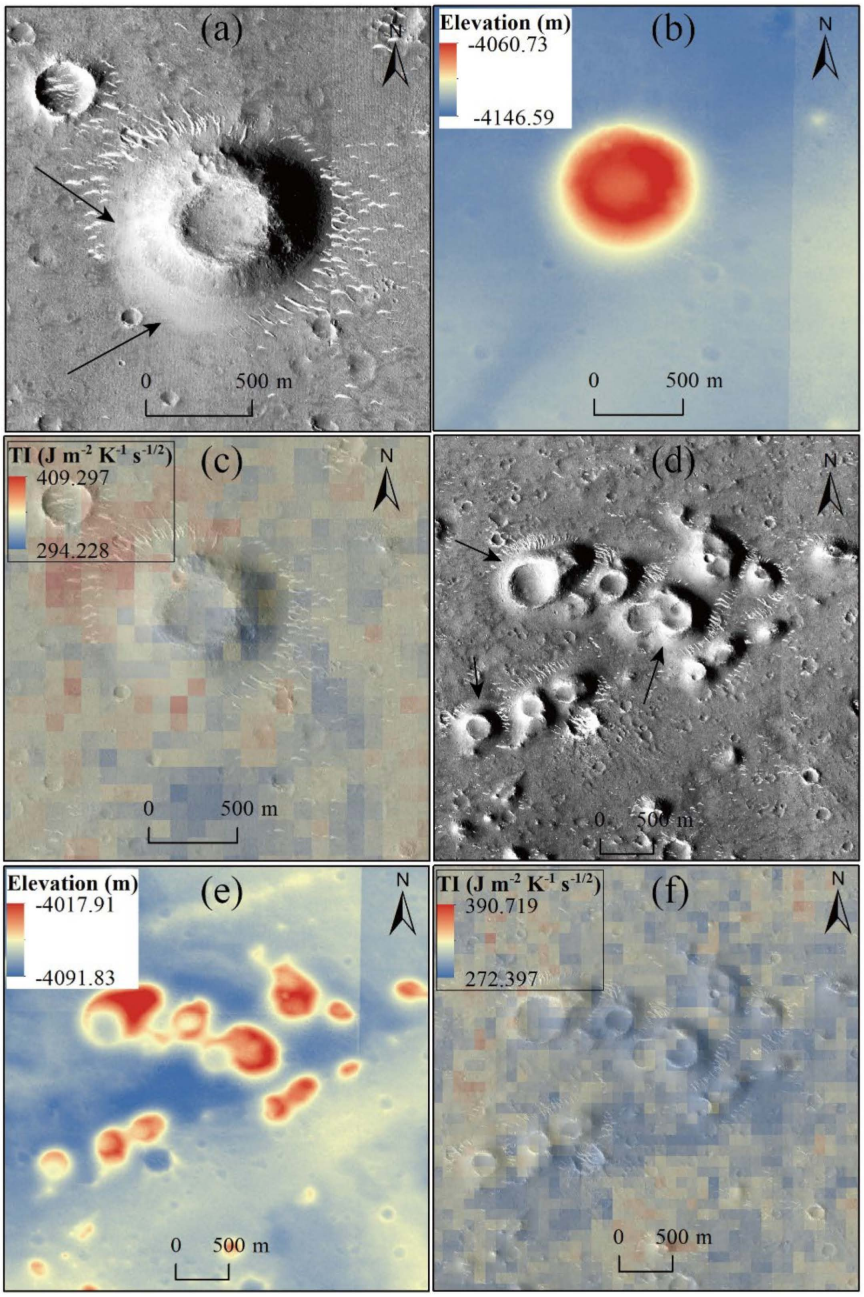

Figure 6. Examples of the landing area cones. (**a**,**d**) are the HiRIC DOM images, (**b**,**e**) are the corresponding HiRIC DEM data, and (**c**,**f**) are the THEMIS−derived TI maps overlaying the panels (**a**,**d**), respectively. Black arrows denote the smooth and fine distinct materials associated with cones compared to the surrounding plains.

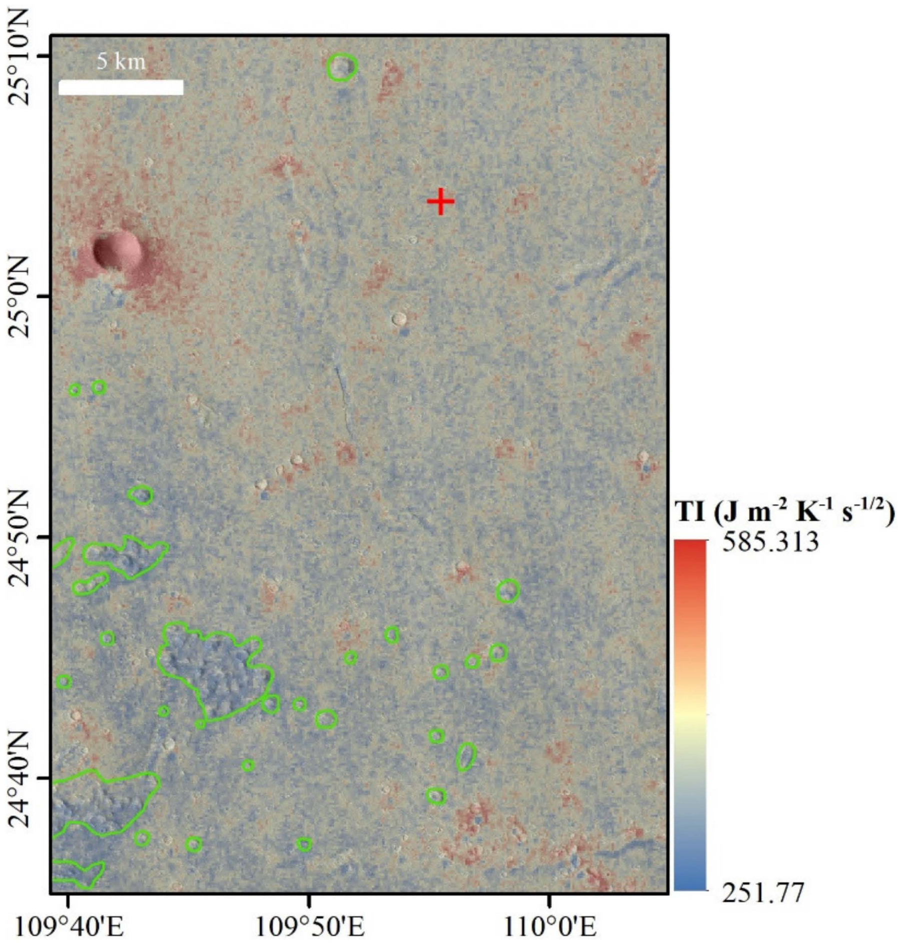

Figure 7. THEMIS−derived thermal inertia map of the landing area. This map overlays the HiRIC DOM, showing the surface physical nature characteristics around the Zhurong landing site. Green lines outlined the cone fields, which present lower TI values. The red cross represents the Zhurong landing site.

3.3. Spatial Analysis

Figure 8a shows the total of 272 measured cones within the landing area of ~8478.6 km^2. These cones are widespread in the study area. The rose diagram (Figure 8b) shows that most cones are located in the clockwise SE-WNW direction area of the landing area. Our studied cones exhibit a clustering pattern according to the observation of their spatial distribution. The NN ratio of 0.6 for all studied cones confirms the clustering of the cones in the landing area and the high $|c|$ values (c = −12.6) attest that this clustering is statistically significant at the 0.05 level [41]. As described by Burno et al. [41], the clustering features (NN ratio < 1) are more closely spaced than would be expected from a random spatial distribution; these clustering features imply that their spatial distribution was systematically controlled by nonrandom processes. The NN analysis of this work reveals a clustering pattern of the studied cones consistent with the case of nonrandom process-controlled feature distribution. The underlying lava pathway geometry and substrate hydrology often create systematically controlled processes [42], which may also provide physical constraints on the formation of the landing area cones.

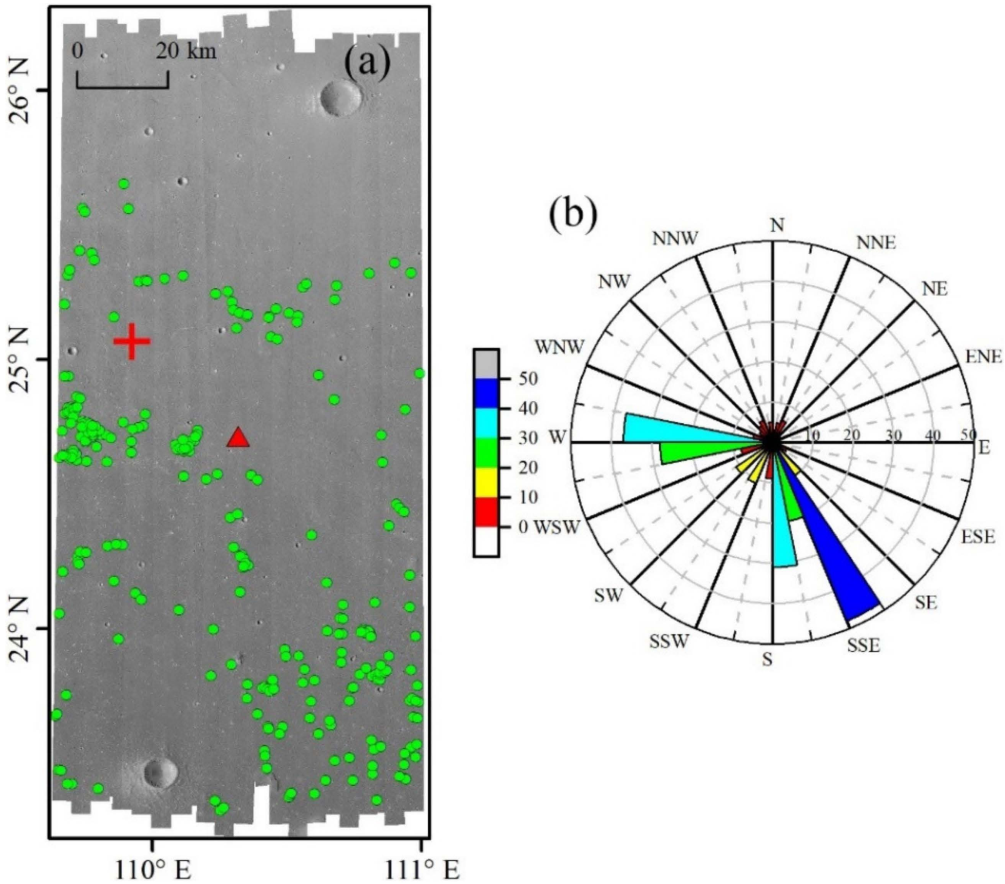

Figure 8. (**a**) Spatial distribution of the landing area cones. Green dots represent the cones. The red cross indicates the Zhurong landing site. (**b**) Rose diagram of the distribution of the landing area cones with 15° bin intervals indicates the number of cones in every separate region. The center of the rose diagram is consistent with the geometric center of the landing area (denoted by red triangle).

Bruno et al. [41] used the skewness-kurtosis relation of pairwise NN distances to add the ability to separate small feature types. In our work, we considered an additional small feature type of mud volcanoes. We acquired the accessible spatial location information of the Martian mud volcanoes reported by [3,5]. Thus, the skewness-kurtosis relationship of Martian mud volcanoes was derived. As shown in Figure 9, the skewness-kurtosis relationship of Martian mud volcanoes (mean kurtosis = 3.75, mean skewness = 1.92) is different from other features (e.g., terrestrial rootless cones, terrestrial ice mounds, rootless cones and ice mounds on Mars, Martian impact craters). For cones in the landing area, the kurtosis and skewness are 4.02 and 1.99, respectively. This result is consistent with Martian mud volcanoes. The unambiguous differences in the skewness–kurtosis relation between the landing area cones and Martian ice mounds/rootless cones also suggested that the pingos or rootless cones are less likely origins of the cones in the landing area.

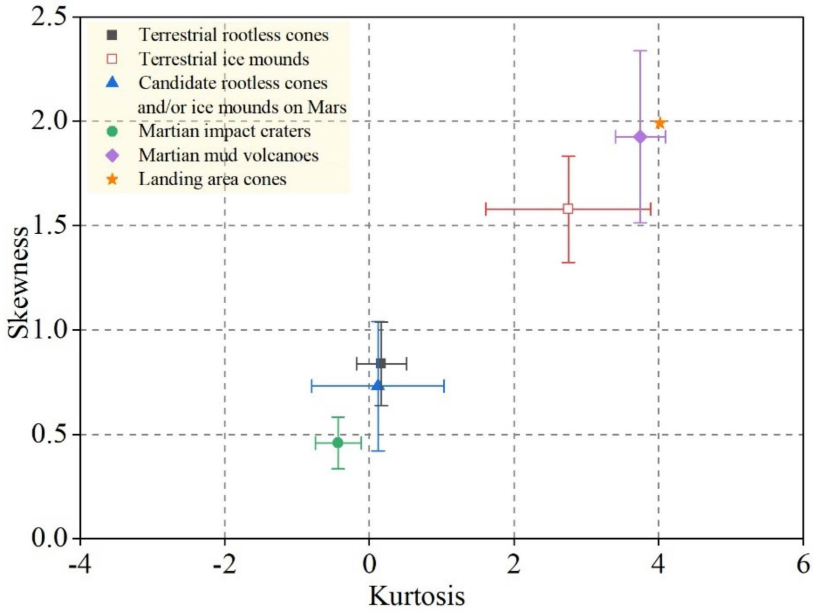

Figure 9. The result of skewness−kurtosis analysis. The error bars are 2 standard errors of the mean. Except for the landing area cones and Martian mud volcanoes, all the other data are from [41]. We calculated the values of Martian mud volcanoes based on their spatial location data from [3,5]. Note, Burno et al. [41] used "ice mound" to replace "pingo".

3.4. Possible Origin of the Cones

The above analyses and discussions suggest two major possible origins for the landing area cones, which are mud volcanoes and igneous-related constructs. In terms of the comparative study with analogous features on Mars (Figure 5a), in addition to mud volcanoes, the morphometric parameters of our studied cones are also similar to a type of igneous cones (Figure S1e,f in Supplementary Materials). This type of igneous cones reported by Dapremont and Wray [40] has a pyroclastic origin. Pyroclastic cones represent many volcanic landforms with various morphometric parameters, including cinder cones, spatter cones, tuff rings/cones, and maars [67]. They are usually interpreted as explosive eruptions productions surrounded by typical lava flows [45]. Geomorphologic features in the landing area are diverse [36]; however, no unambiguous lava flows (or lava tubes, lavas) were observed, and no convincing traces of explosive volcanism (i.e., shield volcanoes, eruptive fissures) were found, which also suggest that the systematic clustering of the cones in the landing area is more likely to be affected by substrate hydrology. For example, the clustering spring-related features (or mud volcanoes) linked to groundwater upwelling in Arabia Terra, as described by Pozzobon et al. [68]. Although Mills et al. [69] interpreted the observed lobate margins as past lava or mud flow boundaries based on the preliminary regional geomorphologic map of the Tianwen-1 Zhurong landing region, it is unclear which type is the exact one. Additionally, previous studies have also suggested the presence of mud volcanism in southern Utopia Planitia [6,26]. Figure 10 shows the linear regression relationships of the three parameters and compares the studied cones with the pyroclastic cones (putative scoria cones) reported by Brož et al. [45]. The relations suggested by Brož et al. [45] are Hco = 0.133 Wco and Wcr = 0.277 Wco, which are different from those of our studied cones (Hco = 0.07023 Wco and Wcr = 0.50137 Wco).

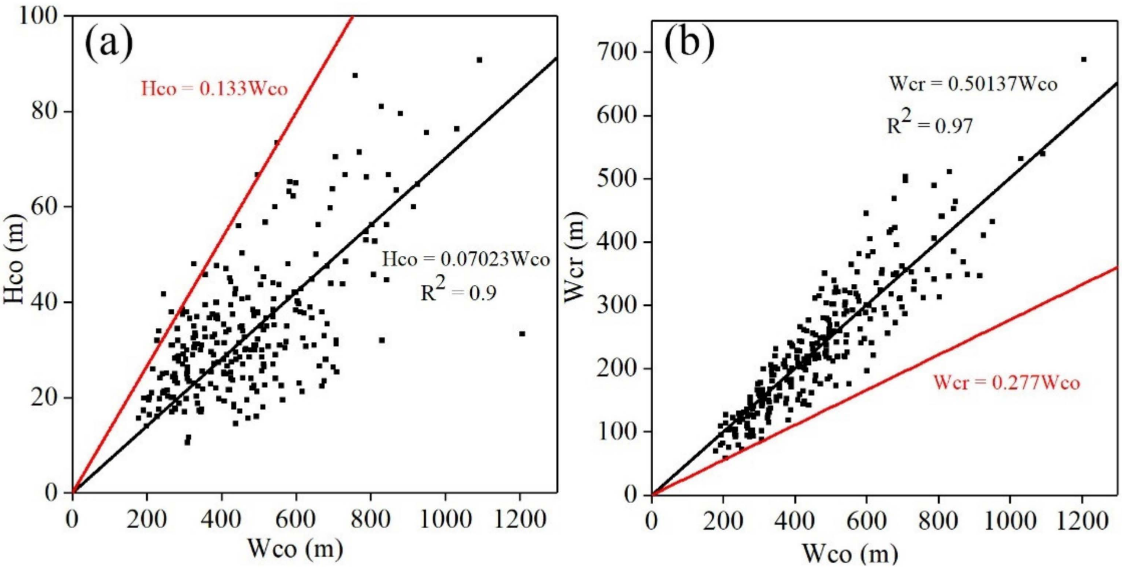

Figure 10. The linear regression relationships of the three parameters. (**a**) Plot of cone height (Hco) versus cone basal diameter (Wco) for the 272 cones. (**b**) Plot of cone crater width (Wcr) versus cone basal diameter (Wco) for the 272 cones. Black lines represent the best fit (linear regression). Red lines represent the best fit from [45].

In terms of comparison with terrestrial features (Figure 5b), the morphometric parameters of pingos, subaqueous/subaerial mud volcanoes, cinder/scoria cones, and rootless cones are relatively consistent with those of the landing area cones. Here, we mainly discuss the hypotheses that were not described and initially ruled out above. Lava domes are generally domical structures with associated lava units [70], which is not the case with the landing area cones. Terrestrial lava domes with an average height of 82.75 m are significantly higher than the cones in this study, and the aspect ratio (Hco/Wco) of lava domes is ~3 times larger than that of landing area cones. In addition, the Martian lava domes reported by Rampery et al. [71] have a mean Hco of 160 m, a mean Wco of 1550 m, and a mean Hco/Wco ratio of 0.11, which are different from those of the landing area cones. Maars are volcanic craters/cones with topographic rims that are significantly different from the landing area cones, and no actual Martian maars have been currently reported [3]. Terrestrial maars have higher Hco and Wco values (mean Hco = 34.36, mean Wco = 1899.69) than the values of the landing area cones (mean Hco = 34.2, mean Wco = 468.3). As described by Brož et al. [10], the thin Martian atmosphere and low gravity are expected to create wider but lower volcanic cones than on Earth. Hence, the morphometric parameters of the Martian cones originating from explosive eruption volcanism will be distinct. This is another reason we exclude that our studied cones formed from phreatomagmatic explosions (e.g., tuff rings/cones, maars, cinder/scoria cones). With regard to terrestrial rootless cones, they are relatively similar to the studied cones (Figure 5b and Figure S1d in Supplementary Materials). As we mentioned above, rootless cones are less likely to be the origins of the cones in the landing area. Rootless cones are generally with raised rims along the edges of the summit pits and are associated with lava flows [12], the shapes of which are different from the landing area cones. Terrestrial subaqueous and subaerial mud volcanoes have a wide range of Hco and Wco but also cover the studied cones.

Concerning the wider geological context, both volcanism and sedimentation are believed to have essential contributions to the geological evolution history of the Martian northern lowlands [30–32,72]. The gravity anomaly model also suggested that Utopia Planitia could be filled with volcanic and sedimentary materials [73]. The landing area is within the lHl (Late Hesperian lowland, lHl) unit [36] that was described as the integrated products of fluvial, sedimentation, and volcanism [74]. Various landforms around the Zhurong landing site also imply volcanism and volatiles release [36,69,75,76], particularly the observed rampart craters that may indicate the subsurface volatiles (water/ice). Hence, the landing area may be the region to support the presence of mud or igneous volcanism.

In summary, morphological evidence, surface physical properties, and spatial analysis results provide more positive hints to support the landing area cones being mud volcanoes rather than volcanic/igneous cones. The landing area cones mentioned in Sections 3.1 and 3.2 are similar to the Type 1 mud volcanoes, which are generally smooth steep-sided cones with a summit crater [4,5]. However, there are no flow-like features, the typical features in mud volcanism fields, along the periphery of the landing area cones. One of the reasonable explanations, as described by Brož et al. [5], is that once the mud is ejected into the Martian atmosphere, it will become dry due to the physical instability of liquid water, and then the mud flow will not form in the local region. This is why the authors explained the absence of flow-like features associated with Type 1 mud volcanoes in their study area. Alternatively, subsequent wind processes (or resurfacing events) can easily modify (or bury) these fine-grained materials. In addition, the igneous interpretation could not be totally ruled out. Although the current observed area is not a typical volcanism zone, it does not mean that there was no volcanism prior to the resurfacing events (e.g., the emplacement of VBF). It is also difficult to provide the additional compositional analysis (e.g., mafic materials, hydrated materials, etc.) to distinguish the mud or igneous volcanic origin due to dust cover and the lack of high-quality spectral image coverage.

3.5. Implications for Future Work

As alluded to in Section 1, the Zhurong rover landed in a geologically complex region. In this work, the current analysis and evidence suggested that the landing area cones are probably related to Martian mud volcanism. Mud volcanoes are generally built with a mixture of gas, liquid water, and sediments [3,5] that originated from depth [77]. Currently, the Zhurong rover is traveling south [36]. Most of the cones are located in the southern part of the landing area (Figure 8a), and the closest cone field along the rover's traveling path is ~16 km away from the landing site. The cones in the landing area will be the long-term targets during the Zhurong rover entering the extended mission phase [36]. There are six playloads on the Zhurong rover [78]. For the landing area cones and their surrounding areas, the MarSCoDe (Mars Surface Composition Detector, MarSCoDe) and the MSCam (Multispectral Camera, MSCam) will reveal the compositions of the features, surrounding geological context, and the surface texture [36,78]. The fine-scale morphology, particle sizes of the surface materials, and properties of minerals will help distinguish between multiple formation hypotheses for the landing area cones. In addition, the powerful tool RoPeR (Mars Rover Penetrating Radar, RoPeR) will investigate the subsurface water/ice of the landing area [78], which will provide insight into the paleoenvironment and substrate hydrology of the landing area. This prospective information will restrict the local geological background of the landing area and the formation scenarios of the landing area cones.

Additionally, the potential substrate hydrology may systematically control the spatial distribution of the landing area cones, as mentioned. Thus, the possible plumbing systems and depth of the possible pressurized reservoir can be assessed combined with self-similar clustering analysis, fractal analysis, and in situ investigation [68].

4. Conclusions

This paper presents a detailed investigation of the TW-1 landing area cones. Based on the HiRIC-derived DOM and DEM data, a total of 272 cones within the landing area were identified to examine their morphologies, morphometrical parameters, spatial characteristics, and surface physical properties. Current evidence favors interpreting the cones in the landing area as Martian mud volcanoes: (1) the ranges of morphometrical parameters of the studied cones are consistent with those of the mud volcanoes on Mars and Earth; (2) the TI values of the landing area cones are lower than those of their surroundings; (3) nonrandom processes (possible substrate hydrology) systematically control the spatial distribution of the landing area cones, and the skewness-kurtosis relationship of these cones is also similar to that of mud volcanoes; (4) the geological settings also support the presence of mud volcanism in the landing area.

Nevertheless, we still leave open the possibility of some igneous volcanic origin, giv-en that it is hard to accurately assess the inconsistency between the studied cones and the other analog features due to various factors (e.g., gravity, atmospheric conditions, for-mation ages, erosion rates, physical properties of soil underlying the cones) [3]. Future work is needed to access the additional evidence. The in situ investigation of the Zhurong rover will provide new insights into the local geological background of the landing area. Such results will help guide future robotic exploration, providing a significant new understanding of the northern ancient ocean hypothesis.

Supplementary Materials: The following supporting information can be downloaded at: https://www.mdpi.com/article/10.3390/rs14112590/s1, Figure S1: Separate panels of Figure 5; Table S1: Morphometric parameters and locations of the 272 cones measured in this study.

Author Contributions: Conceptualization, H.H. and J.L.; methodology, H.H. and J.L.; writing—original draft preparation, H.H.; writing—review and editing, H.H., J.L. and X.W.; data curation Q.Z., Y.C., X.R., W.Y. and D.L. All authors have read and agreed to the published version of the manuscript.

Funding: This study was supported by the Key Research Program of the Chinese Academy of Sciences (Grant NO. ZDBS-SSW-TLC001).

Institutional Review Board Statement: Not applicable.

Informed Consent Statement: Not applicable.

Data Availability Statement: All HiRIC data used in this paper are available at https://moon.bao.ac.cn/web/enmanager/zygj (accessed on 2 October 2021). Datasets generated or analyzed during this study are available from the corresponding author upon reasonable request. The Themis-derived map presented in this study can be found here: https://astrogeology.usgs.gov/maps/mars-themis-derived-global-thermal-inertia-mosaic (accessed on 2 January 2022).

Acknowledgments: This work was supported by the China National Space Administration (CNSA). We thank the team members of the Tianwen-1 mission: the probe system, the launch vehicle system, the launch site system, the Telemetry Track and Command System and the Ground Research and Application System.

Conflicts of Interest: The authors declare no conflict of interest.

References

1. Allen, C.C. Volcano–Ice Interactions on Mars. *J. Geophys. Res. Solid Earth* **1979**, *84*, 8048–8059. [CrossRef]
2. Frey, H.; Lowry, B.L.; Chase, S.A. Pseudocraters on Mars. *J. Geophys. Res. Solid Earth* **1979**, *84*, 8075–8086. [CrossRef]
3. Hemmi, R.; Miyamoto, H. Distribution, Morphology, and Morphometry of Circular Mounds in the Elongated Basin of Northern Terra Sirenum, Mars. *Prog. Earth Planet. Sci.* **2017**, *4*, 26. [CrossRef]
4. Komatsu, G.; Okubo, C.H.; Wray, J.J.; Ojha, L.; Cardinale, M.; Murana, A.; Orosei, R.; Chan, M.A.; Ormö, J.; Gallagher, R. Small Edifice Features in Chryse Planitia, Mars: Assessment of a Mud Volcano Hypothesis. *Icarus* **2016**, *268*, 56–75. [CrossRef]
5. Brož, P.; Hauber, E.; van de Burgt, I.; Špillar, V.; Michael, G. Subsurface Sediment Mobilization in the Southern Chryse Planitia on Mars. *J. Geophys. Res. Planets* **2019**, *124*, 703–720. [CrossRef]
6. Ivanov, M.A.; Hiesinger, H.; Erkeling, G.; Reiss, D. Mud Volcanism and Morphology of Impact Craters in Utopia Planitia on Mars: Evidence for the Ancient Ocean. *Icarus* **2014**, *228*, 121–140. [CrossRef]
7. Brož, P.; Hauber, E. Hydrovolcanic Tuff Rings and Cones as Indicators for Phreatomagmatic Explosive Eruptions on Mars. *J. Geophys. Res. Planets* **2013**, *118*, 1656–1675. [CrossRef]
8. De Pablo, M.Á.; Komatsu, G. Possible Pingo Fields in the Utopia Basin, Mars: Geological and Climatical Implications. *Icarus* **2009**, *199*, 49–74. [CrossRef]
9. Dundas, C.M.; McEwen, A.S. An Assessment of Evidence for Pingos on Mars Using HiRISE. *Icarus* **2010**, *205*, 244–258. [CrossRef]
10. Brož, P.; Čadek, O.; Hauber, E.; Rossi, A.P. Scoria Cones on Mars: Detailed Investigation of Morphometry Based on High-Resolution Digital Elevation Models. *J. Geophys. Res. Planets* **2015**, *120*, 1512–1527. [CrossRef]
11. Meresse, S.; Costard, F.; Mangold, N.; Masson, P.; Neukum, G. Formation and Evolution of the Chaotic Terrains by Subsidence and Magmatism: Hydraotes Chaos, Mars. *Icarus* **2008**, *194*, 487–500. [CrossRef]
12. Noguchi, R.; Kurita, K. Unique Characteristics of Cones in Central Elysium Planitia, Mars. *Planet. Space Sci.* **2015**, *111*, 44–54. [CrossRef]

13. Hamilton, C.W.; Fagents, S.A.; Thordarson, T. Lava–Ground Ice Interactions in Elysium Planitia, Mars: Geomorphological and Geospatial Analysis of the Tartarus Colles Cone Groups. *J. Geophys. Res. Planets* **2011**, *116*, 3004. [CrossRef]
14. Hargitai, H.; Kereszturi, Á. (Eds.) *Encyclopedia of Planetary Landforms*; Springer: New York, NY, USA, 2015. [CrossRef]
15. Sánchez-Bayton, M.; Herraiz, M.; Martin, P.; Sánchez-Cano, B.; Tréguier, E.; Kereszturi, A. Morphological Analyses of Small and Medium Size Landforms in Scandia Cavi and Olympia Undae, Northern Circumpolar Region of Mars. *Planet. Space Sci.* **2022**, *210*, 105389. [CrossRef]
16. Komatsu, G. Rivers in the Solar System: Water Is Not the Only Fluid Flow on Planetary Bodies. *Geogr. Compass* **2007**, *1*, 480–502. [CrossRef]
17. Plescia, J.B. Cinder cones of Isidis and Elysium. *NASA Tech. Memo* **1980**, *82385*, 263–265.
18. Frey, H.; Jarosewich, M. Subkilometer Martian Volcanoes: Properties and Possible Terrestrial Analogs. *J. Geophys. Res. Solid Earth* **1982**, *87*, 9867–9879. [CrossRef]
19. Keszthelyi, L.P.; Jaeger, W.L.; Dundas, C.M.; Martínez-Alonso, S.; McEwen, A.S.; Milazzo, M.P. Hydrovolcanic Features on Mars: Preliminary Observations from the First Mars Year of HiRISE Imaging. *Icarus* **2010**, *205*, 211–229. [CrossRef]
20. McGill, G.E. Buried Topography of Utopia, Mars: Persistence of a Giant Impact Depression. *J. Geophys. Res. Solid Earth* **1989**, *94*, 2753–2759. [CrossRef]
21. Thomson, B.J.; Head, J.W. Utopia Basin, Mars: Characterization of Topography and Morphology and Assessment of the Origin and Evolution of Basin Internal Structure. *J. Geophys. Res. Planets* **2001**, *106*, 23209–23230. [CrossRef]
22. Hiesinger, H.; Head, J.W. Characteristics and Origin of Polygonal Terrain in Southern Utopia Planitia, Mars: Results from Mars Orbiter Laser Altimeter and Mars Orbiter Camera Data. *J. Geophys. Res. Planets* **2000**, *105*, 11999–12022. [CrossRef]
23. Buczkowski, D.L.; Seelos, K.D.; Cooke, M.L. Giant Polygons and Circular Graben in Western Utopia Basin, Mars: Exploring Possible Formation Mechanisms. *J. Geophys. Res. Planets* **2012**, *117*, 8010. [CrossRef]
24. Séjourné, A.; Costard, F.; Swirad, Z.M.; Łosiak, A.; Bouley, S.; Smith, I.; Balme, M.R.; Orgel, C.; Ramsdale, J.D.; Hauber, E.; et al. Grid Mapping the Northern Plains of Mars: Using Morphotype and Distribution of Ice-Related Landforms to Understand Multiple Ice-Rich Deposits in Utopia Planitia. *J. Geophys. Res. Planets* **2019**, *124*, 483–503. [CrossRef]
25. Orgel, C.; Hauber, E.; van Gasselt, S.; Reiss, D.; Johnsson, A.; Ramsdale, J.D.; Smith, I.; Swirad, Z.M.; Séjourné, A.; Wilson, J.T.; et al. Grid Mapping the Northern Plains of Mars: A New Overview of Recent Water- and Ice-Related Landforms in Acidalia Planitia. *J. Geophys. Res. Planets* **2019**, *124*, 454–482. [CrossRef]
26. Skinner, J.A.; Tanaka, K.L. Evidence for and Implications of Sedimentary Diapirism and Mud Volcanism in the Southern Utopia Highland–Lowland Boundary Plain, Mars. *Icarus* **2007**, *186*, 41–59. [CrossRef]
27. Lanz, J.K.; Wagner, R.; Wolf, U.; Kröchert, J.; Neukum, G. Rift Zone Volcanism and Associated Cinder Cone Field in Utopia Planitia, Mars. *J. Geophys. Res. Planets* **2010**, *115*. [CrossRef]
28. Soare, R.J.; Costard, F.; Pearce, G.D.; Séjourné, A. A Re-Interpretation of the Recent Stratigraphical History of Utopia Planitia, Mars: Implications for Late-Amazonian Periglacial and Ice-Rich Terrain. *Planet. Space Sci.* **2012**, *60*, 131–139. [CrossRef]
29. Costard, F.; Sejourne, A.; Kargel, J.; Godin, E. Modeling and Observational Occurrences of Near-Surface Drainage in Utopia Planitia, Mars. *Geomorphology* **2016**, *275*, 80–89. [CrossRef]
30. Head, J.W.; Kreslavsky, M.A.; Pratt, S. Northern Lowlands of Mars: Evidence for Widespread Volcanic Flooding and Tectonic Deformation in the Hesperian Period. *J. Geophys. Res. Planets* **2002**, *107*, 3–1–3–29. [CrossRef]
31. Parker, T.J.; Gorsline, D.S.; Saunders, R.S.; Pieri, D.C.; Schneeberger, D.M. Coastal Geomorphology of the Martian Northern Plains. *J. Geophys. Res. Planets* **1993**, *98*, 11061–11078. [CrossRef]
32. Parker, T.J.; Stephen Saunders, R.; Schneeberger, D.M. Transitional Morphology in West Deuteronilus Mensae, Mars: Implications for Modification of the Lowland/Upland Boundary. *Icarus* **1989**, *82*, 111–145. [CrossRef]
33. Head, J.W.; Hiesinger, H.; Ivanov, M.A.; Kreslavsky, M.A.; Pratt, S.; Thomson, B.J. Possible Ancient Oceans on Mars: Evidence from Mars Orbiter Laser Altimeter Data. *Science* **1999**, *286*, 2134–2137. [CrossRef] [PubMed]
34. Pan, L.; Ehlmann, B.L.; Carter, J.; Ernst, C.M. The Stratigraphy and History of Mars' Northern Lowlands through Mineralogy of Impact Craters: A Comprehensive Survey. *J. Geophys. Res. Planets* **2017**, *122*, 1824–1854. [CrossRef]
35. Tanaka, K.L.; Banerdt, W.B.; Kargel, J.S.; Hoffman, N. Huge, CO2-charged debris-flow deposit and tectonic sagging in the northern plains of Mars. *Geology* **2001**, *29*, 427–430. [CrossRef]
36. Liu, J.; Li, C.; Zhang, R.; Rao, W.; Cui, X.; Geng, Y.; Jia, Y.; Huang, H.; Ren, X.; Yan, W.; et al. Geomorphic Contexts and Science Focus of the Zhurong Landing Site on Mars. *Nat. Astron.* **2021**, *6*, 65–71. [CrossRef]
37. Gilichinsky, M.; Demidov, N.; Rivkina, E.; Gilichinsky, M.; Demidov, N.; Rivkina, E. Morphometry of Volcanic Cones on Mars in Perspective of Astrobiological Research. *IJAsB* **2015**, *14*, 537–545. [CrossRef]
38. Domagal-Goldman, S.D.; Wright, K.E.; Adamala, K.; Arina de la Rubia, L.; Bond, J.; Dartnell, L.R.; Goldman, A.D.; Lynch, K.; Naud, M.-E.; Paulino-Lima, I.G.; et al. The Astrobiology Primer v2.0. *AsBio* **2016**, *16*, 561–653. [CrossRef]
39. Yan, W.; Liu, J.; Ren, X.; Li, C.; Fu, Q.; Wang, D.; Dong, J.; Zhang, X.; Chen, W.; Tan, X.; et al. Detection Capability Verification and Performance Test for the High Resolution Imaging Camera of China's Tianwen-1 Mission. *Space Sci. Rev.* **2021**, *217*, 71. [CrossRef]
40. Dapremont, A.M.; Wray, J.J. Igneous or Mud Volcanism on Mars? The Case Study of Hephaestus Fossae. *J. Geophys. Res. Planets* **2021**, *126*, e2020JE006390. [CrossRef]

41. Bruno, B.C.; Fagents, S.A.; Hamilton, C.W.; Burr, D.M.; Baloga, S.M. Identification of Volcanic Rootless Cones, Ice Mounds, and Impact Craters on Earth and Mars: Using Spatial Distribution as a Remote Sensing Tool. *J. Geophys. Res. Planets* **2006**, *111*. [CrossRef]
42. Bruno, B.C.; Fagents, S.A.; Thordarson, T.; Baloga, S.M.; Pilger, E. Clustering within Rootless Cone Groups on Iceland and Mars: Effect of Nonrandom Processes. *J. Geophys. Res. Planets* **2004**, *109*, 7009. [CrossRef]
43. Baloga, S.M.; Glaze, L.S.; Bruno, B.C. Nearest-Neighbor Analysis of Small Features on Mars: Applications to Tumuli and Rootless Cones. *J. Geophys. Res. Planets* **2007**, *112*, 3002. [CrossRef]
44. Clark, P.J.; Evans, F.C. Distance to Nearest Neighbor as a Measure of Spatial Relationships in Populations. *Ecology* **1954**, *35*, 445–453. [CrossRef]
45. Brož, P.; Hauber, E. A Unique Volcanic Field in Tharsis, Mars: Pyroclastic Cones as Evidence for Explosive Eruptions. *Icarus* **2012**, *218*, 88–99. [CrossRef]
46. Favalli, M.; Karátson, D.; Mazzarini, F.; Pareschi, M.T.; Boschi, E. Morphometry of Scoria Cones Located on a Volcano Flank: A Case Study from Mt. Etna (Italy), Based on High-Resolution LiDAR Data. *J. Volcanol. Geotherm. Res.* **2009**, *186*, 320–330. [CrossRef]
47. Wood, C.A. Morphometric Analysis of Cinder Cone Degradation. *J. Volcanol. Geotherm. Res.* **1980**, *8*, 137–160. [CrossRef]
48. Mustard, J.F.; Cooper, C.D.; Rifkin, M.K. Evidence for Recent Climate Change on Mars from the Identification of Youthful Near-Surface Ground Ice. *Nature* **2001**, *412*, 411–414. [CrossRef]
49. Head, J.W.; Mustard, J.F.; Kreslavsky, M.A.; Milliken, R.E.; Marchant, D.R. Recent Ice Ages on Mars. *Nature* **2003**, *426*, 797–802. [CrossRef]
50. Dundas, C.M.; Mellon, M.T.; McEwen, A.S.; Lefort, A.; Keszthelyi, L.P.; Thomas, N. HiRISE Observations of Fractured Mounds: Possible Martian Pingos. *Geophys. Res. Lett.* **2008**, *35*. [CrossRef]
51. Burr, D.M.; Tanaka, K.L.; Yoshikawa, K. Pingos on Earth and Mars. *Planet. Space Sci.* **2009**, *57*, 541–555. [CrossRef]
52. Cabrol, N.A.; Grin, E.A.; Pollard, W.H. Possible Frost Mounds in an Ancient Martian Lake Bed. *Icarus* **2000**, *145*, 91–107. [CrossRef]
53. Hasenaka, T.; Carmichael, I.S.E. The Cinder Cones of Michoacán—Guanajuato, Central Mexico: Their Age, Volume and Distribution, and Magma Discharge Rate. *J. Volcanol. Geotherm. Res.* **1985**, *25*, 105–124. [CrossRef]
54. Pike, R.J. Volcanoes on the inner planets—Some preliminary comparisons of gross topography. In Proceedings of the Lunar and Planetary Science Conference Proceedings, Houston, TX, USA, 13–17 March 1978; pp. 3239–3273.
55. Rodríguez, S.R.; Morales-Barrera, W.; Layer, P.; González-Mercado, E. A Quaternary Monogenetic Volcanic Field in the Xalapa Region, Eastern Trans-Mexican Volcanic Belt: Geology, Distribution and Morphology of the Volcanic Vents. *J. Volcanol. Geotherm. Res.* **2010**, *197*, 149–166. [CrossRef]
56. Kioka, A.; Ashi, J. Episodic Massive Mud Eruptions from Submarine Mud Volcanoes Examined through Topographical Signatures. *Geophys. Res. Lett.* **2015**, *42*, 8406–8414. [CrossRef]
57. Kirkham, C.; Cartwright, J.; Hermanrud, C.; Jebsen, C. The Spatial, Temporal and Volumetric Analysis of a Large Mud Volcano Province within the Eastern Mediterranean. *Mar. Pet. Geol.* **2017**, *81*, 1–16. [CrossRef]
58. Chigira, M.; Tanaka, K. Structural features and the history of mud volcanoes in southern Hokkaido, northern Japan. *J. Geol. Soc. Jpn.* **1997**, *103*, 781–791. [CrossRef]
59. Oehler, D.Z.; Allen, C.C. Evidence for Pervasive Mud Volcanism in Acidalia Planitia, Mars. *Icarus* **2010**, *208*, 636–657. [CrossRef]
60. Ghent, R.R.; Anderson, S.W.; Pithawala, T.M. The Formation of Small Cones in Isidis Planitia, Mars through Mobilization of Pyroclastic Surge Deposits. *Icarus* **2012**, *217*, 169–183. [CrossRef]
61. Fergason, R.L.; Christensen, P.R.; Kieffer, H.H. High-Resolution Thermal Inertia Derived from the Thermal Emission Imaging System (THEMIS): Thermal Model and Applications. *J. Geophys. Res. Planets* **2006**, *111*. [CrossRef]
62. Christensen, P.R.; Fergason, R.L.; Edwards, C.S.; Hill, J. THEMIS-derived thermal inertia mosaic of Mars: Product description and science results. In Proceedings of the 44th Annual Lunar and Planetary Science Conference, The Woodlands, TX, USA, 18–22 March 2013; p. 2822.
63. Fergason, R.L.; Christensen, P.R.; Bell, J.F.; Golombek, M.P.; Herkenhoff, K.E.; Kieffer, H.H. Physical Properties of the Mars Exploration Rover Landing Sites as Inferred from Mini-TES–Derived Thermal Inertia. *J. Geophys. Res. Planets* **2006**, *111*. [CrossRef]
64. Senthil Kumar, P.; Krishna, N.; Prasanna Lakshmi, K.J.; Raghukanth, S.T.G.; Dhabu, A.; Platz, T. Recent Seismicity in Valles Marineris, Mars: Insights from Young Faults, Landslides, Boulder Falls and Possible Mud Volcanoes. *Earth Planet. Sci. Lett.* **2019**, *505*, 51–64. [CrossRef]
65. Farrand, W.H.; Gaddis, L.R.; Keszthelyi, L. Pitted Cones and Domes on Mars: Observations in Acidalia Planitia and Cydonia Mensae Using MOC, THEMIS, and TES Data. *J. Geophys. Res. Planets* **2005**, *110*, 1–14. [CrossRef]
66. Salvatore, M.R.; Christensen, P.R. On the Origin of the Vastitas Borealis Formation in Chryse and Acidalia Planitiae, Mars. *J. Geophys. Res. Planets* **2014**, *119*, 2437–2456. [CrossRef]
67. Brož, P. Pyroclastic Cone. *Encycl. Planet. Landf.* **2015**, 1660–1664. [CrossRef]
68. Pozzobon, R.; Mazzarini, F.; Massironi, M.; Rossi, A.P.; Pondrelli, M.; Cremonese, G.; Marinangeli, L. Fluids Mobilization in Arabia Terra, Mars: Depth of Pressurized Reservoir from Mounds Self-Similar Clustering. *Icarus* **2019**, *321*, 938–959. [CrossRef]
69. Mills, M.M.; McEwen, A.S.; Okubo, C.H. A Preliminary Regional Geomorphologic Map in Utopia Planitia of the Tianwen-1 Zhurong Landing Region. *Geophys. Res. Lett.* **2021**, *48*, e2021GL094629. [CrossRef]

70. Brož, P.; Hauber, E.; Platz, T.; Balme, M. Evidence for Amazonian Highly Viscous Lavas in the Southern Highlands on Mars. *Earth Planet. Sci. Lett.* **2015**, *415*, 200–212. [CrossRef]
71. Rampey, M.L.; Milam, K.A.; McSween, H.Y.; Moersch, J.E.; Christensen, P.R. Identity and Emplacement of Domical Structures in the Western Arcadia Planitia, Mars. *J. Geophys. Res. Planets* **2007**, *112*, 6011. [CrossRef]
72. Tanaka, K.L.; Skinner, J.A.; Hare, T.M.; Joyal, T.; Wenker, A. Resurfacing History of the Northern Plains of Mars Based on Geologic Mapping of Mars Global Surveyor Data. *J. Geophys. Res. Planets* **2003**, *108*, E4. [CrossRef]
73. Zuber, M.T. Internal Structure and Early Thermal Evolution of Mars from Mars Global Surveyor Topography and Gravity. *Science* **2000**, *287*, 1788–1793. [CrossRef]
74. Tanaka, K.L.; Skinner, J.A.; Dohm, J.M.; Irwin, R.P., III; Kolb, E.J.; Fortezzo, C.M.; Platz, T.; Michael, G.G.; Hare, T.M. *Geologic Map of Mars: Pamphlet to Accompany Scientific Investigations Map 3292*; U.S. Geological Survey: Reston, VA, USA, 2014. [CrossRef]
75. Ye, B.; Qian, Y.; Xiao, L.; Michalski, J.R.; Li, Y.; Wu, B.; Qiao, L. Geomorphologic exploration targets at the Zhurong landing site in the southern Utopia Planitia of Mars. *Earth Planet. Sci. Lett.* **2021**, *576*, 117199. [CrossRef]
76. Wu, X.; Liu, Y.; Zhang, C.; Wu, Y.; Zhang, F.; Du, J.; Liu, Z.; Xing, Y.; Xu, R.; He, Z.; et al. Geological Characteristics of China's Tianwen-1 Landing Site at Utopia Planitia, Mars. *Icarus* **2021**, *370*, 114657. [CrossRef]
77. Kopf, A.J. Significance of mud volcanism. *Rev. Geophys.* **2002**, *40*, 2–1–2–52. [CrossRef]
78. Li, C.; Zhang, R.; Yu, D.; Dong, G.; Liu, J.; Geng, Y.; Sun, Z.; Yan, W.; Ren, X.; Su, Y.; et al. China's Mars Exploration Mission and Science Investigation. *Space Sci. Rev.* **2021**, *217*, 57. [CrossRef]